MNRAS **000**, 000–000 (0000) Preprint 12 March 2022 Compiled using MNRAS LATEX style file v3.0

Discriminating Local Sources of High-Energy Cosmic Electrons and Positrons by Current and Future Anisotropy Measurements

Kun Fang[1,2] , Xiao-Jun Bi[1,2], Peng-Fei Yin[1]
[1] *Key Laboratory of Particle Astrophysics, Institute of High Energy Physics, Chinese Academy of Sciences, Beijing 100049, China*
[2] *School of Physical Sciences, University of Chinese Academy of Sciences, Beijing 100049, China*

12 March 2022

ABSTRACT

The Fermi-LAT detects no significant anisotropy of the cosmic-ray (CR) electrons and positrons ($e^- + e^+$) with seven years of data, which provides the strongest restriction to the $e^- + e^+$ anisotropy up to now. As next generation CR observatory, HERD is expected to have a better capability of anisotropy detection than Fermi-LAT. In this paper, we discuss several models aimed to explain the AMS-02 data by the present and future anisotropy measurements. We find that the upper limits of Fermi-LAT disfavor Vela SNR as the dominant source in sub-TeV, while other cases that remain safe under the constraint of Fermi-LAT are expected to be distinguished from each other by HERD. We then discuss the possibilities of remarkable TeV spectral features, and test the corresponding anisotropies. We find the conditions under which the TeV model can have a prominent spectral feature and avoid the constraint of Fermi-LAT at the same time. Furthermore, the expected performance of HERD is sensitive enough to detect the anisotropies of all these TeV models, and even for the case of a featureless TeV spectrum. Thus HERD may play a crucial part in the study of the origin of cosmic electrons and positrons.

1 INTRODUCTION

The AMS-02 collaboration has respectively obtained the cosmic-ray (CR) electron and positron ($e^{\pm}$) spectra (Aguilar et al. 2014), owing to the strong capability of the sign-of-charge discrimination. These measurements provide stronger constraints on theoretical models of the cosmic lepton origin, compared with merely the measurement of the electron plus positron ($e^- + e^+$) spectrum. The high-precision results of AMS-02 not only confirm the existence of the $e^{\pm}$ excess detected by the previous experiments (Chang et al. 2008; Adriani et al. 2009), but also indicate that the electron spectrum has a larger excess than that of the positron (Feng et al. 2014; Li et al. 2015; Lin et al. 2015). This extra excess of electrons can be interpreted as the spectral fluctuation brought by discrete local supernova remnants (SNRs) (Lin et al. 2015).

After the work of Shen (1970), many astrophysical models have been proposed, in which nearby SNRs are calculated separately from background SNRs (Atoyan et al. 1995; Kobayashi et al. 2004; Di Mauro et al. 2014), in order to explain the CR observations. Along this approach, we have carefully investigated local CR sources and discussed their parameters of electron injection, to fit all the leptonic data of AMS-02, and give predictions to $e^- + e^+$ spectrum beyond 1 TeV (Fang et al. 2017, hereafter F17). Vela SNR is traditionally believed to be the most important local source around TeV, while other candidates also have the possibility to explain the extra electron excess. Although the possible candidates to explain the AMS-02 data are few (Fang et al. 2017), the current leptonic data of AMS-02 cannot discriminate among them.

However, things may be different when the anisotropy in the arrival direction of cosmic electrons is taken into account. Even two sources produce similar leptonic spectra, the angular distributions would be different due to their different positions. Also, the magnitude of the anisotropy of these sources may also be different. Therefore the anisotropy measurement can provide an unprecedentedly strong constraint on theoretical models. Linden & Profumo (2013) depicted the prospective of ascertaining the origin of the pulsar account for the positron excess, by the anisotropy measurement of atmospheric Cherenkov telescopes. More recently, Manconi et al. (2017) performed a detailed analysis of local CR $e^{\pm}$ sources, and presented the corresponding anisotropies.

In March 2017, the Fermi-LAT collaboration published the latest result of anisotropy measurement with seven years of data (Abdollahi et al. 2017). As no significant anisotropy has been detected in any angular scale, Fermi-LAT provides the strongest upper limits of anisotropy so far. Furthermore, the future Chinese Space Station based instrument HERD (the High Energy Cosmic-Radiation Detector) aims to measure the energy spectrum and anisotropy of $e^- + e^+$ up to

10 TeV (HERD, Zhang et al. 2014). HERD is planned to be launched before 2025 with more than 10 years of lifetime and is expected to have a better sensitivity than Fermi-LAT.

In this work we discuss the possibility to discriminate the local sources of high energy $e^{\pm}$ by combining the leptonic spectra and the current or future anisotropy measurements. Our work has several important differences with the previous studies, such as Manconi et al. (2017). First, we calculate the total anisotropies of theoretical models, including the anisotropy of the SNR background. The background component also contributes considerably to the total anisotropy and should not be omitted in the calculation. Second, when Vela cannot account for the electron excess, we adopt specific sources like Monogem Ring or Loop I as the dominant local source in sub-TeV to explain the AMS-02 data. Third, we also discuss possible spectral features generated by local sources above TeV, together with their anisotropies. Finally, we adopt not only the latest anisotropy limits given by Fermi-LAT, but also the expected HERD sensitivity in the model discussions.

This paper is organized as follows. In Section 2, we review the $e^{\pm}$ sources in our framework and the propagation of $e^{\pm}$; then we introduce the calculation of the total anisotropies of theoretical models, and the expectation of the sensitivity of HERD. In Section 3, we first discuss the models aimed to explain the AMS-02 data with the anisotropy limits of Fermi-LAT and the expected sensitivity of HERD; then we calculate the anisotropies corresponding to several models with remarkable TeV spectral features, and compare them with the anisotropy measurements. We give some discussions on other possibilities in Section 4, and then conclude in the last section.

2 METHOD

2.1 Injection and Propagation of Galactic $e^{\pm}$

In F17, we have already described our calculation of $e^{\pm}$ spectra at the Earth in detail, so in the following we just give a brief introduction to the injection spectrum of $e^{\pm}$ sources and the propagation of CR $e^{\pm}$. In our framework, SNRs are the main contributors of CR electrons, while pulsar wind nebulae (PWNe) provide both high energy positrons and electrons. Secondary positrons are considered as the background of the positron spectrum.

For SNRs, the injection spectrum of electrons can be expressed as

$$Q(E) = Q_0 (E/1\,\mathrm{GeV})^{-\gamma} \exp(-E/E_c)\,, \qquad (1)$$

where Q_0 is the normalization of the injection spectrum, γ is the power-law spectral index, and E_c is the cut-off energy. We divide SNRs into a group of known young and local sources and a background component with a continuous distribution. The background SNRs share a common injection spectrum. Their $Q_{0,\mathrm{bkg}}$ and γ_{bkg} are determined by the fitting procedures in the next section, and E_c is set to be 20 TeV. The local SNRs adopted in this work are shown in Table 1. Considering the age and distance of these individual SNRs, only three of them—Vela YZ, Loop I, and Monogem Ring—can potentially contribute to the electron excess in the sub-TeV region (F17). We leave the discussion of these three sources in the next section. For other SNRs, we constrain their parameters of the injection spectrum by multi-band electromagnetic observations, or just radio observations in the absence of X-ray and γ-ray measurements. One may refer to F17 for the detailed processes.

Name	$l(^\circ)$	$b(^\circ)$	r(kpc)	t(kyr)
G65.3+5.7	65.3	+5.7	0.8	28
Cygnus Loop	74.0	−8.5	0.54	10
G114.3+0.3	114.3	+0.3	0.7	7.7
R5	127.1	+0.5	1.00	25
G156.2+5.7	156.2	+5.7	1.00	20.5
HB9	160.9	+2.6	0.8	5.5
Vela Jr.	266.2	−1.2	0.75	3
RX J1713.7-3946	347.3	−0.5	1.00	1.6
Vela YZ	263.9	−3.3	0.29	11.3
Monogem Ring	203.0	+12.0	0.3	86
Loop I (NPS)	328.3	+17.6	0.1	200

Table 1. The name, location, distance, and age of SNRs within 1 kpc. One can refer to Di Mauro et al. (2014) and references therein for parameters of these sources; while for Monogem Ring and Loop I, their distance and age listed here are taken from Plucinsky (2009) and Egger & Aschenbach (1995) respectively.

The injection spectrum for the PWN case takes the same form with equation (1), while PWNe can provide both electrons and positrons. As in F17, we adopt a single powerful PWN to explain the high energy positron spectrum of AMS-02. The only difference is that we choose Geminga as the single PWN in the present work, rather than Monogem. The characteristic age, distance, and spin-down luminosity of Geminga pulsar are $t = 342$ kyr, $r = 250$ pc, and $\dot{E} = 3.25 \times 10^{34}$ erg s^{-1}, respectively (Manchester et al. 2005). The total spin-down luminosity can be derived by $W_{\mathrm{pwn}} = \dot{E} t (1 + t/\tau_0) = 1.23 \times 10^{49}$ erg, where the spin-down time scale τ_0 is set to be 10 kyr. The normalization of the injection spectrum is decided by W_{pwn} and η_{pwn}, the latter of which is the efficiency of energy conversion to the injected electrons and positrons. We set η_{pwn} and the spectral index γ_{pwn} as free parameters in the following fitting procedures. The calculation of secondary positrons keeps the same with that in F17.

The propagation of Galactic $e^{\pm}$ can be described by the diffusion equation with consideration of energy loss during their journey:

$$\frac{\partial N}{\partial t} - \nabla(D \nabla N) - \frac{\partial}{\partial E}(bN) = Q\,, \qquad (2)$$

where N is the number density of $e^{\pm}$, D denotes the diffusion coefficient, b denotes the energy-loss rate, and Q is the source function. The diffusion coefficient D has the form of $D(E) = \beta D_0 (R/1\,\mathrm{GV})^{\delta}$, where D_0 and δ are both constants, β is the velocity of particles in the unit of light speed and R is the rigidity of CRs. In this work, the diffusion coefficient refers to the DR2 model of Yuan et al. (2017), in which $D_0 = (2.08 \pm 0.28) \times 10^{28}$ cm^2 s^{-1}, $\delta = 0.500 \pm 0.012$. The energy-loss rate is given by $b(E) = -b_0(E) E^2$, where $b_0(E)$

is decided by synchrotron and inverse Compton radiation of CR $e^{\pm}$. We follow the method of Schlickeiser & Ruppel (2010) to calculate the inverse Compton term, while we set the interstellar magnetic field in the Galaxy to be 1 μG to get the synchrotron term (Han & Qiao 1994; Delahaye et al. 2010).

Equation (2) can be solved with the method of Green's function (Ginzburg & Syrovatskii 1964). We adopt the spherically symmetric solution, which is safe for the case of high energy $e^{\pm}$ (Kobayashi et al. 2004). To determine the source function, local SNRs and PWNe are considered as point sources with burst-like injection. For the background SNRs, we assume a smooth spatial distribution derived by Lorimer (2004), and the SN explosion rate is set to be $f = 4$ century^{-1} galaxy^{-1} (Delahaye et al. 2010). The critical distance and age between local and background SNRs are set to be $r_m = 1$ kpc and $t_m = 3 \times 10^5$ years respectively as what we do in F17.

2.2 Anisotropy of Electrons and Positrons

Presupposing the dipolar distribution of the intensity of CRs, the anisotropy of CRs is generally defined as

$$\Delta = \frac{I_{\rm max} - I_{\rm min}}{I_{\rm max} + I_{\rm min}}\,, \tag{3}$$

where $I_{\rm max}$ and $I_{\rm min}$ are the maximum and minimum values of the CR intensity at the Earth, respectively. If we take a specific form of the angular distribution of the CR intensity from a source as

$$I_i(\boldsymbol{n}) = \bar{I}_i(1 + \Delta_i\, \boldsymbol{n}_i \cdot \boldsymbol{n})\,, \tag{4}$$

where $\bar{I}_i = (I_{i,\rm max} + I_{i,\rm min})/2$, $\boldsymbol{n}_i$ is the direction of the source, and Δ_i denotes the anisotropy of that source, then under the diffusion model, equation (3) can be rewritten as

$$\Delta_i = \frac{3D}{c} \cdot \frac{|\nabla N_i|}{N_i}\,, \tag{5}$$

which is derived by Ginzburg & Syrovatskii (1964). Combining equation (5) and the solution of a point source with burst-like injection, we get the explicit expression of the $e^{\pm}$ anisotropy of a single source with distance r_i and age t_i:

$$\Delta_i = \frac{3D}{c} \cdot \frac{2r_i}{\lambda_i^2}\,, \tag{6}$$

where

$$\lambda_i^2 = 4 \int_E^{\frac{E}{1-b_0 E t_i}} \frac{D(E')}{b(E')} dE' \tag{7}$$

describes the propagation distance of $e^{\pm}$ with arrival energy E. If $E \ll 1/(b_0 t_i)$, the diffusion scale can be approximated by $\lambda_i = 2\sqrt{D\, t_i}$. For a source with age of 10 kyr, this approximation only brings a relative error of several percent to the anisotropy even in TeV range. Under this approximation, equation (6) has a form of

$$\Delta_i = \frac{3r_i}{2ct_i}\,, \tag{8}$$

in which the anisotropy is simply decided by the age and distance of the source. We still adopt equation (6) to calculate the anisotropy in the following, but we should keep in mind that the anisotropy only has a weak dependence on the diffusion coefficient D.

In order to comparing theoretical models with experimental data, it is essential to calculate the total anisotropy contributed by all the sources in each model. The total intensity is given by summation of equation (4):

$$I(\boldsymbol{n}) = \sum_i \bar{I}_i(1 + \Delta_i \boldsymbol{n}_i \cdot \boldsymbol{n})\,. \tag{9}$$

Then the total anisotropy can be obtained from the definition of equation (3):

$$\Delta = \frac{\sum \bar{I}_i \Delta_i \boldsymbol{n}_i \cdot \boldsymbol{n}_{\rm max}}{\sum \bar{I}_i}\,, \tag{10}$$

where $\boldsymbol{n}_{\rm max}$ is the direction of the maximum intensity. For the local SNRs, their locations can be found in the Green catalog. As to pulsars, their Galactic longitudes l and latitudes b are given in the ATNF catalog. Equation (10) indicates that the contribution of an individual source to the total anisotropy is related to its relative intensity compared with the total intensity, rather than its absolute intensity.

Since the distribution of distant SNRs is symmetric around the Galactic center but not the solar system, and they also have significant contribution to the electron spectrum, we emphasize that the SNR background should be a considerable component in the calculation of the total anisotropy. We treat the SNR background component as a whole, so its anisotropy may also be calculated by equation (5):

$$\Delta_{\rm bkg} = \frac{3D}{c} \cdot \frac{1}{N_{\rm bkg}} \cdot \left| \frac{N_{\rm bkg}(r_\odot + \Delta r) - N_{\rm bkg}(r_\odot - \Delta r)}{2\Delta r} \right|\,, \tag{11}$$

where $N_{\rm bkg}$ is the number density of the background SNR. The difference step Δr is set to be 0.1 kpc, and a smaller Δr makes little difference to the result. The location of the background component is $l = 0$, $b = 0$, and hence the direction vector in the rectangular coordinate is $\boldsymbol{n}_{\rm bkg} = \{1, 0, 0\}$.

For each model in the following, we need to find $\boldsymbol{n}_{\rm max}$ in different energies. We calculate $I(l, b)$ for every $1^\circ \times 1^\circ$ grid to find the maximum $I(l, b)$ and thus obtain $\boldsymbol{n}_{\rm max}$. The positions of all our local SNRs are listed in Table 1, while the location of PWNe discussed in the following sections can be found in Table 4.

2.3 Expected Sensitivity of HERD

HERD is a next generation CR observatory onboard China's Space Station, and is planned for operation starting around 2025 for about 10 years. One of the main scientific objectives of HERD is the precise and direct measurements of the $e^- + e^+$ spectrum and the anisotropy up to 10 TeV. Here we give an expectation on the sensitivity of $e^- + e^+$ detection of HERD, and we will show in the following sections that the anisotropy measurement of HERD can play an important role in the study of CR $e^{\pm}$ origin.

We briefly summarize the baseline performance of HERD first; one can refer to Zhang et al. (2014, 2017); Dong et al. (2017) for details. The main instrument of HERD is a 3-D cubic calorimeter (CALO). It is composed of thousands of small cubic crystals, and is surrounded by microstrip silicon trackers from five sides except the bottom. This novel design brings HERD an effective geometrical factor of > 3 m^2 sr, which is 10 times larger than the previous

Energy [GeV]	100	200	500	750	1000
A [m^2 sr]	3.38	3.28	3.18	3.13	3.10

Table 2. Geometrical acceptance of HERD for $e^{\pm}$ at different energies.

CR detectors in space. The large geometrical factor is the biggest advantage of HERD, and it is the key parameter for the detection of anisotropy. The geometrical acceptances at different energies are shown in Table 2[1]. Besides, by using 3-d imaging of the shower of the particle event, the average electron/proton (e/p) discrimination between 100 GeV and 1 TeV is expected to reach 10^6, which is much better than that of Fermi-LAT. HERD will measure the $e^- + e^+$ spectrum from 100 MeV to 10 TeV, with an energy resolution of 1% at 100 GeV.

We then estimate the sensitivity of $e^- + e^+$ detection of HERD. The detected number of $e^- + e^+$ can be calculated by $N = A\,t\,\bar{I}(E)\,\Delta E$, where A is the energy dependent geometrical acceptance, which is obtained by interpolation or extrapolation with the data in Table 2. The operation time is denoted with t, and ΔE is the width of energy bins taken to be 0.3 in logarithmic scale. The flux of $e^- + e^+$ is taken as the theoretical $e^- + e^+$ spectrum in each theoretical model. The relative systematic uncertainty is simply $1/\sqrt{N}$, while the systematic uncertainty mainly arises from the misidentification of other particles as $e^{\pm}$ (Pato et al. 2010). We calculate the relative systematic uncertainty by $(N_p/N_e)/(e/p)$, where N_p is the proton flux, N_e is the flux of $e^- + e^+$, and e/p is 10^6 as described above. We adopt the proton flux measured by AMS-02 (Aguilar et al. 2015), and find the relative systematic uncertainty is in $\sim 10^{-4}$. Thus the error is dominated by the statistical one, and the minimum detectable anisotropy at 2σ can be estimated by $2/\sqrt{N}$.

3 RESULTS

In F17 we have proposed several models to fit the AMS-02 data (hereafter referred as the sub-TeV region). In Section 3.1, we emphasize on the corresponding anisotropy predictions of these models and show how the present and future measurements of anisotropy can constrain or discriminate among these models. Then the possibilities of prominent spectral features above TeV (hereafter referred as the TeV region) are discussed in Section 3.2, and the corresponding anisotropies are tested.

3.1 Sub-TeV Region

In the following, Vela YZ, Loop I, and Monogem Ring are taken as the predominant SNR in sub-TeV respectively. As described in the previous section, some of the parameters are decided by the global fitting to the four groups of leptonic data of AMS-02. However, for the sake of brevity, only the $e^- + e^+$ spectrum of each model is shown in the following figures.

3.1.1 Vela YZ

Vela SNR is believed to be the most promising local electron source, since its appropriate age and distance and its strong radio flux may lead to a significant contribution to the electron spectrum (Kobayashi et al. 2004; Di Mauro et al. 2014). Vela SNR mainly consists of a PWN—Vela X, and two shell structure—Vela Y and Vela Z (Rishbeth 1958). We do not include Vela X here since it cannot help to explain the extra excess of electrons compared with positrons, due to its PWN nature (Weiler & Panagia 1980). In this model, we take some typical parameters for Vela YZ: a magnetic field of 30 μG, a cut-off energy of 2 TeV, and a radio flux of 1000 Jy at 1 GHz. The spectral index $\gamma_{\rm vela}$ is left to be free as it is a crucial parameter to the dominance of Vela YZ but still with large uncertainty in observation. We seek the best-fit model by minimizing chi-square statistic between model and AMS-02 leptonic spectra[2]. The best-fit parameters of this subsection are all listed in Table 3.

Figure 1 shows the best-fit $e^- + e^+$ spectrum, the corresponding anisotropy, and the angular distribution of intensity (to be exact, $[I(l,b) - \bar{I}]/\bar{I} \times 100$) at 100 GeV. As can be seen, although the flux of Vela YZ is smaller than the background component, it still produces such a remarkable anisotropy that the total theoretical anisotropy reaches the exclusion limit at 95% C.L. indicated by Fermi-LAT. Vela YZ leads the anisotropy from around 100 GeV to 1 TeV, above which its anisotropy is somehow offset by that of G65.3+5.7 whose position is opposite to Vela YZ. Vela YZ dominates the anisotropy not only because its considerable flux of electrons, but also its relatively large r/t ratio, as explained by equation (8). The result indicates that the upper limits given by Fermi-LAT disfavor Vela YZ as the dominant electron source in sub-TeV. More generally, the extra electron excess in sub-TeV should not be explained by a relatively young SNR like Vela. We also find that the expected sensitivity of three years of HERD data is obviously lower than the theoretical anisotropy of this model, which can give a more convincing judgment to this scenario in the future.

3.1.2 Monogem Ring

As we introduced in F17, the electron flux of Vela YZ can be much smaller if we investigate a little more on its parameters. Sushch & Hnatyk (2014) derive a magnetic field of 46 μG in the region where Vela YZ is located. A shock velocity of 6×10^7 cm s^{-1} is suggested by Sushch et al. (2011), which leads to $E_c = 4$ TeV (Yamazaki et al. 2006). The latest result of the radio spectrum of Vela Y and Vela Z can be found in Alvarez et al. (2001). Sushch & Hnatyk (2014) merge the radio spectrum of Vela Y and Vela Z and obtain a electron spectral index of 2.47. In this case, the electron flux of Vela YZ is about 10 times less than the previous model, mainly due to the much softer spectral index. To explain the extra excess of electrons, Monogem Ring (MR) is one of the two candidate local SNRs.

MR is considered as the counterpart of pulsar

[1] These are the preliminary result provided by the HERD collaboration.

[2] Steven G. Johnson, The NLopt nonlinear-optimization package, http://ab-initio.mit.edu/nlopt

Model	$\gamma_{\rm bkg}$	$Q_{0,\rm bkg}[10^{50}{\rm GeV}^{-1}]$	$\gamma_{\rm pwn}$	$\eta_{\rm pwn}$	$\gamma_{\rm vela}$	χ^2/d.o.f
Vela	2.42	2.48	1.82	1.80	2.12	0.43

Model	$\gamma_{\rm bkg}$	$Q_{0,\rm bkg}[10^{50}{\rm GeV}^{-1}]$	$\gamma_{\rm pwn}$	$\eta_{\rm pwn}$	$\gamma_{\rm mr}$	$W_{\rm mr}[10^{48}\,{\rm erg}]$	$E_{c,\rm mr}[{\rm TeV}]$	χ^2/d.o.f
Loop I	2.50	3.11	1.79	1.72	1.87	6.29	1.55	0.42

Model	$\gamma_{\rm bkg}$	$Q_{0,\rm bkg}[10^{50}{\rm GeV}^{-1}]$	$\gamma_{\rm pwn}$	$\eta_{\rm pwn}$	$\gamma_{\rm loop}$	$W_{\rm loop}[10^{48}\,{\rm erg}]$	$E_{c,\rm loop}[{\rm TeV}]$	χ^2/d.o.f
MR	2.51	3.35	1.79	1.70	1.93	2.24	1.09	0.42

Table 3. Fitting results of the sub-TeV models. Vela YZ is abbreviated to Vela in this table.

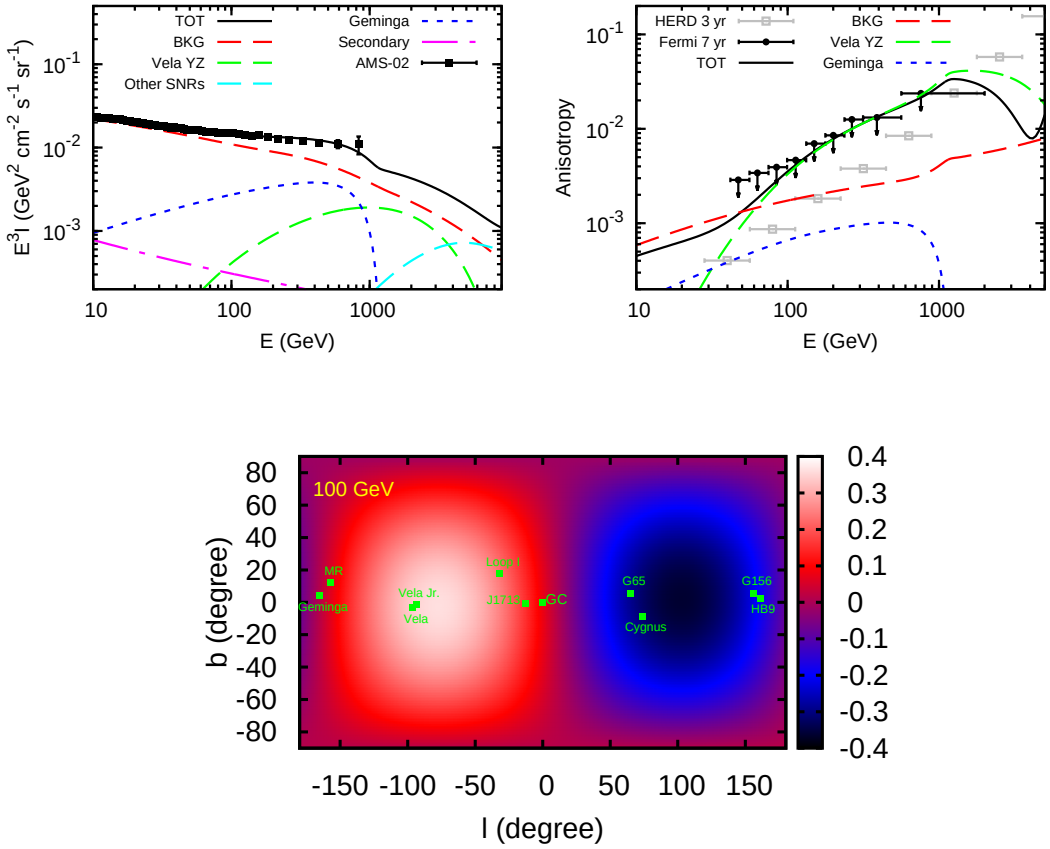

Figure 1. The $e^- + e^+$ spectrum (top left), anisotropy (top right), and the angular distribution of intensity ($[I(l,b) - \bar{I}]/\bar{I} \times 100$) at 100 GeV (bottom) of *Vela YZ* model. In the legend, 'Other SNRs' refers to the summation of our local SNRs except for Vela YZ, Monogem Ring, and Loop I. In the top-right graph, the dash and dotted lines represent for the quantity $\bar{I}_i\Delta_i/\sum \bar{I}_i$. Note $\bar{I}_i\Delta_i/\sum \bar{I}_i$ of 'Other SNRs' are not shown in the bottom graph, but they are included in the calculation of the total anisotropy. For the upper limits of Fermi-LAT, we adopt the result using the log-likelihood ratio method.

B0656+14 which is located 288 pc away (Plucinsky 2009). A distance of ~ 300 pc corresponds to an age of 8.6×10^4 years and an initial explosion energy of 0.19×10^{51} erg, which is estimated by the X-ray observation and the Sedov-Taylor model (Plucinsky et al. 1996). We let the spectral index, total energy, and cut-off energy free in the fitting, and denote them with $\gamma_{\rm mr}$, $W_{\rm mr}$, and $E_{c,\rm mr}$. As can be seen in Table 3, the best-fit electron energy is 2.24×10^{48} erg. Relating this $W_{\rm mr}$ and the initial explosion energy of 0.19×10^{51} erg, a very large conversion efficiency of 10^{-2} is required.

The total anisotropy of this model is smaller than the sensitivity of Fermi-LAT, as shown in Fig. 2. This indicates that the *Monogem Ring* scenario is still safe under the constraint of Fermi-LAT. As can be seen from the top right graph, MR contributes most to the total anisotropy in the sub-TeV region. At 100 GeV, the $\boldsymbol{n}_{\rm max}$ is near the direction of Monogem Ring, which can be found in the bottom graph of Fig. 2. Moreover, the theoretical anisotropy below 200 GeV of this model is larger than the expected sensitivity of

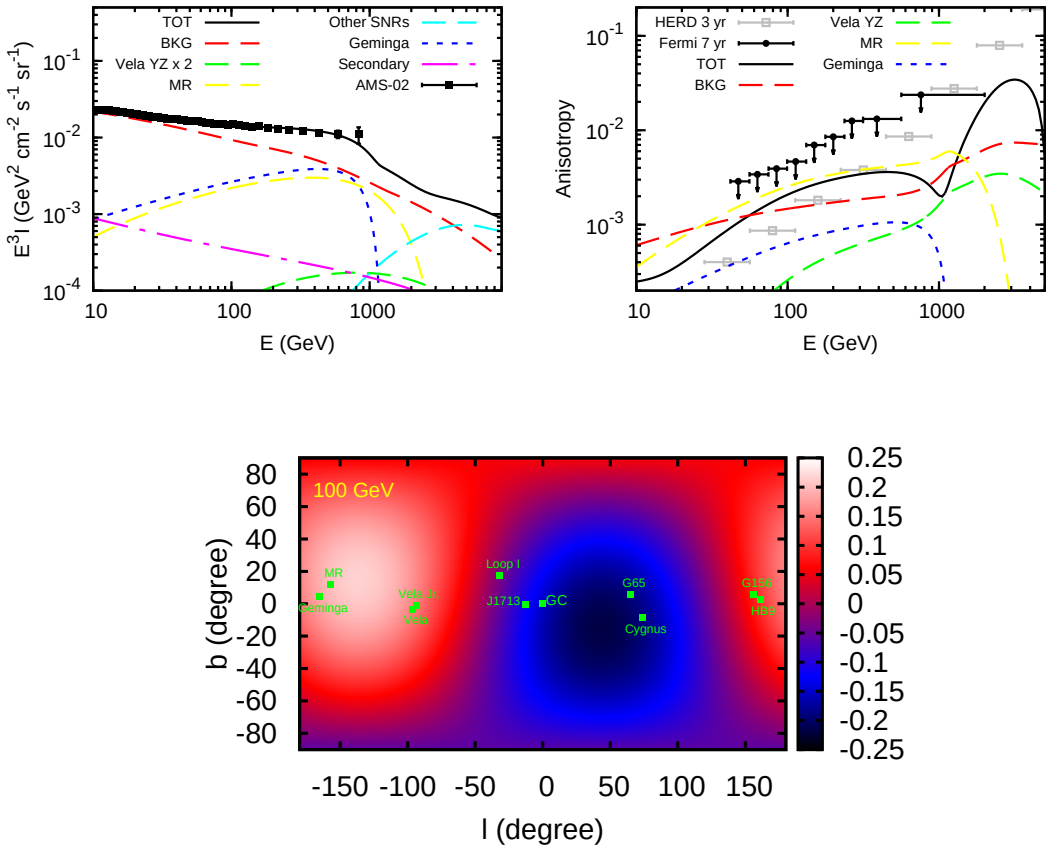

Figure 2. Same as Figure 1, but for the *Monogem Ring* scenario.

HERD with 3 years observation, which means this model may also be tested by HERD.

3.1.3 *Loop I (NPS)*

In addition to MR, Loop I is the other potential electron contributor in sub-TeV, when Vela YZ provides little flux of electrons. Although Loop I is believed to be an old structure ($\sim 10^6$ years) due to the low velocity of neutral gas surrounding it (Sofue et al. 1974), the soft X-ray emission from the interior of Loop I indicates that there may be one or more subsequent SN events in the Sco-Cen association (Borken & Iwan 1977; Egger & Aschenbach 1995), which is located in the center of Loop I . The North Polar Spur (NPS) is the most prominent structure of Loop I, both in radio and X-ray maps, which can be interpreted by the reheating of a recent SN (Egger & Aschenbach 1995). What is more, Fermi-LAT collaboration also detect high energy γ-ray emission in the NPS region and the shape of this excess is similar to those seen in synchrotron emission (Casandjian et al. 2009). This may buttress the reheating picture of Loop I. We set 2×10^5 years as the age of NPS which is suggested by Egger & Aschenbach (1995), and the distance to NPS is 100 pc. Like the previous model, we set $\gamma_{\rm loop}$, $W_{\rm loop}$, and $E_{\rm c,loop}$ as free parameters.

As presented in Fig. 3, the total anisotropy of this model is clearly under the constraint of Fermi-LAT. Below 1 TeV, the anisotropy of this model is dominated by the background SNRs. The contribution of Loop I (NPS) to the total anisotropy is smaller than the background component, because of the old age and close distance of Loop I (NPS). This indicates that the anisotropy of the background SNRs is indeed non-negligible. As shown in the top right of Fig. 3, the total anisotropy below 100 GeV is possible to be detected by HERD with 3 years of observation. At the same time, the angular distribution of intensity at 100 GeV (bottom of Fig. 3) is distinct from that of the *Monogem Ring* scenario, since Monogem Ring locates in almost the opposite direction to the Galactic center. Thus the future measurement of HERD may distinguish between this model and the *Monogem Ring* model.

3.2 TeV Region

The $e^- + e^+$ spectrum above TeV has been measured by several experiments, while there is still inconsistency among these measurements. DAMPE has confirmed a clear spectral break in $\sim$1 TeV (DAMPE Collaboration 2017), which is in agreement with the earlier result of H.E.S.S (Aharonian et al. 2008). Thus we add several TeV sources respectively on a background with a break power-law form to discuss the possible spectral features in the TeV region. For the background, the spectral index below 1 TeV is assumed to be -3.17 as measured by AMS-02, and soften by

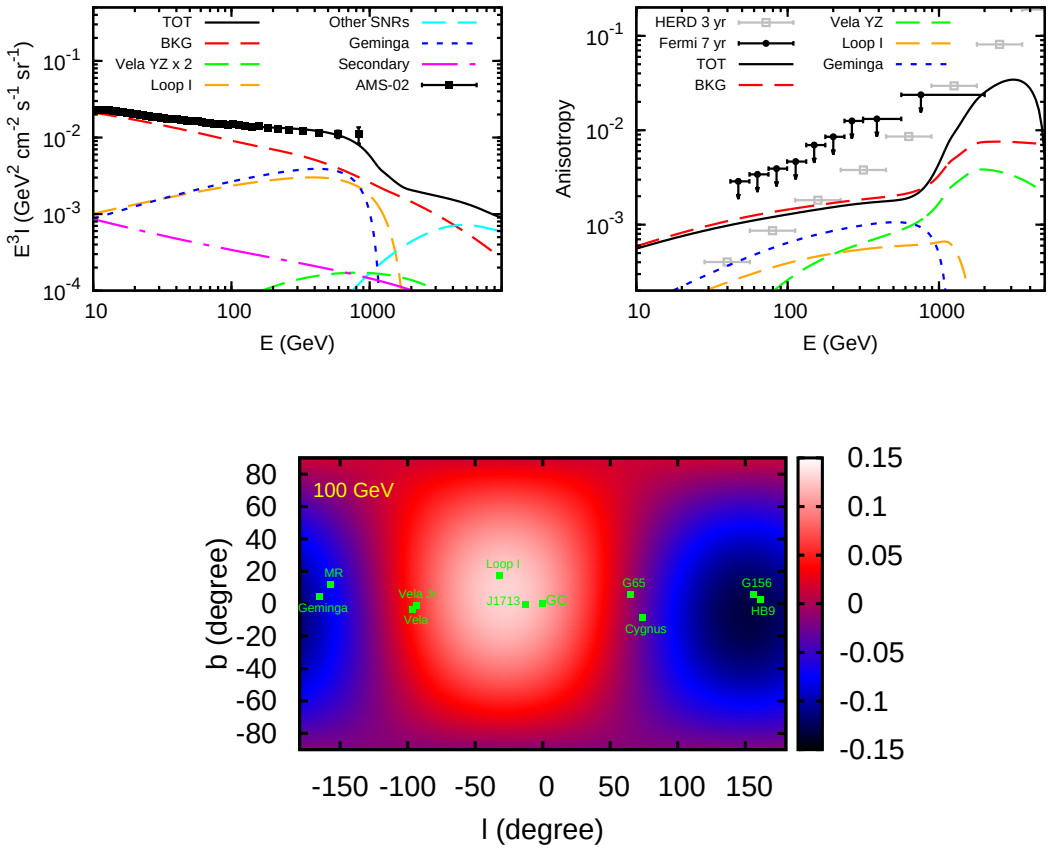

Figure 3. Same as Figure 1, but for the *Loop I (NPS)* scenario.

1 above 1 TeV. The anisotropy is assumed to be dominated by the TeV local sources.

3.2.1 Vela YZ

Kobayashi et al. (2004) have shown the scenario that if we take into account the release time, that is, the time delay of electron injection, Vela YZ can contribute significantly in the TeV region. Particles may begin to escape from the shock front of SNR when the velocity of the shock has dropped to the order of the Alfvén velocity of the ISM (Dorfi 2000). The mean Alfvén velocity of ISM can be calculated by $v_A = 2.18 \times 10^5$ cm s^{-1} $(m_i/m_p)^{-1/2}\,(n_{\rm ISM}/{\rm cm}^{-3})^{-1/2}\,(B/\mu{\rm G})$, where m_i is the ion mass, m_p is the mass of proton, $n_{\rm ISM}$ and $B_{\rm ISM}$ are number density and magnetic field of ISM respectively. The dynamics of expansion of Vela SNR suggests $n_{\rm ISM} \leqslant 0.01$ cm^{-3} (Sushch et al. 2011), and if we assume $B_{\rm ISM}$ to be 10 μG, the Alfvén velocity of the surrounding medium should be $\sim 1 \times 10^7$ cm s^{-1}. The shock velocity of Vela YZ region is observed to be 6×10^7 cm s^{-1} (Sushch et al. 2011), and the shock velocity evolves with $t^{-3/5}$ in Sedov phase. So the initial velocity should be large than 10^8 cm s^{-1}, which is much faster than the Alfvén velocity of ISM. This indicates that a considerable release time for Vela YZ is reasonable.

In this model, we assume a release time of 10 kyr for Vela YZ, which corresponds to a young injection age of 1 kyr. We take a typical value of 2.0 for the injection spectral index of Vela YZ, and the cut-off energy is assumed to be 4 TeV as we explained in the previous subsection. Fig. 4 presents the $e^- + e^+$ spectrum and the anisotropy of this model. The TeV spectrum has a bump feature compared with a power-law form, although Vela YZ does not stand out enough from the background. If the injection age of Vela YZ is larger, its flux of lower energy electrons will increase. Then Vela YZ will be mixed with the background and no remarkable feature is expected. At the same time, the anisotropy of this model conflicts with the upper limit of the last energy bin of Fermi-LAT. The reason is indicated by equation (10): the Δ_i of Vela YZ with such a young injection age is very large (~ 0.7), and the flux of Vela YZ is non-neglectable in sub-TeV.

3.2.2 Vela X

Vela X consists of two component: a halo and a 'cocoon' (de Jager et al. 2008; Hinton et al. 2011). However, the low cut-off energy of 100 GeV for the former and the small total leptonic energy of 10^{46} erg for the later prevent Vela X to create a distinctive spectral feature in TeV region. Hinton et al. (2011) point out that the low cut-off energy for the halo component may be attributed to an energy dependent escape which happens at the time of the crush of the original PWN. They assume a spectral index of 1.8,

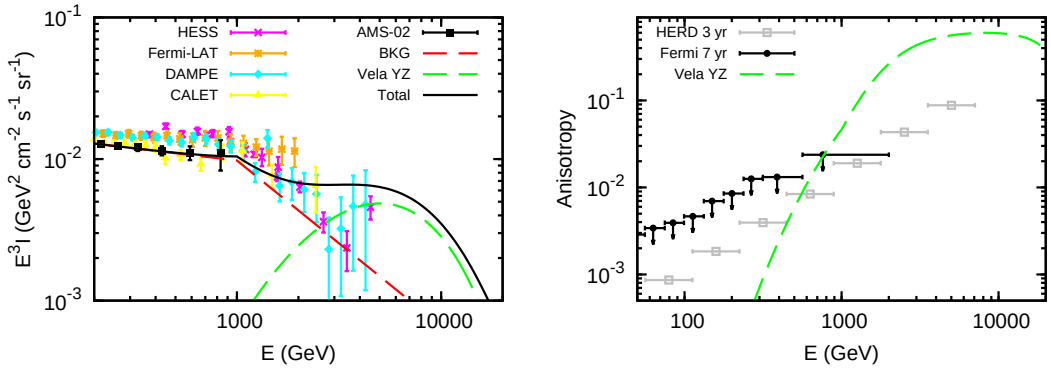

Figure 4. The scenario that Vela YZ produces TeV spectral feature. A considerable injection delay of 10 kyr is assumed. Note the background component is a break power-law spectrum, which has different meaning with that in the figures of Section 3.1.

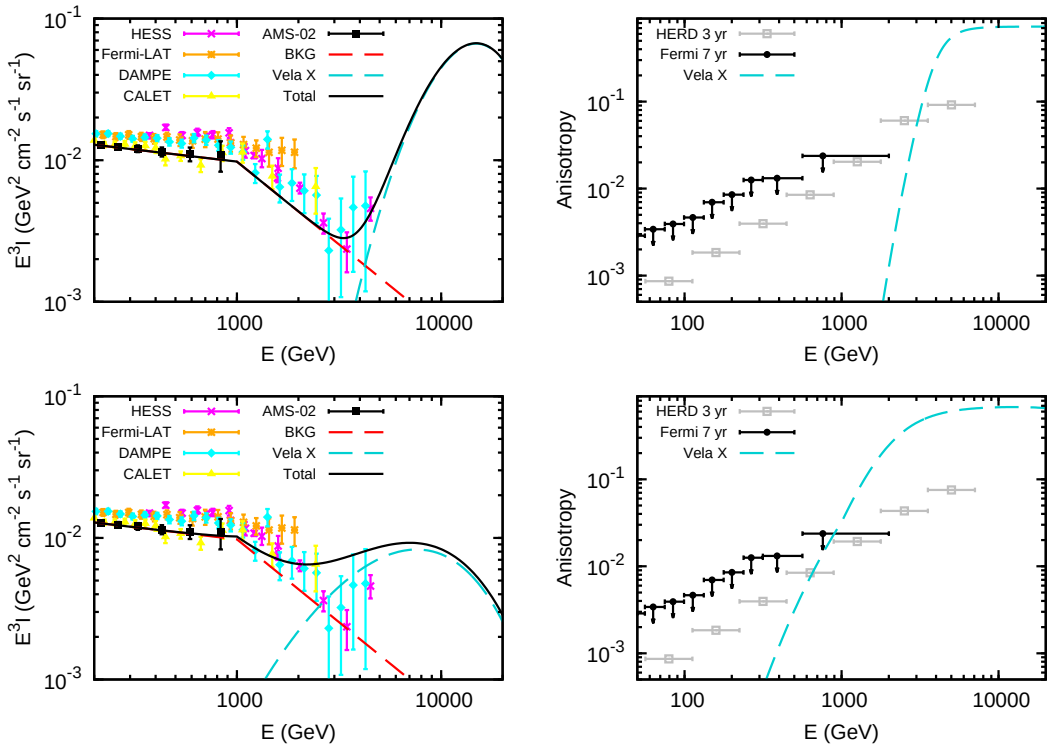

Figure 5. The scenario that Vela X produces TeV spectral feature. Top graphs: the $e^- + e^+$ spectrum and anisotropy spectrum using the model of Hinton et al. (2011), and release time of 7 kyr is adopted; bottom graphs: the same with the top ones, but we use the diffusion coefficient of our own, and assume a leptonic injection energy of 10^{47} erg and a release time of 10 kyr.

a cut-off energy of 6 TeV, and a total leptonic energy of 6.8×10^{48} erg in their model. After considering the release time of electrons, their result shows that Vela X can produce a prominent TeV spectrum of $e^- + e^+$. Nevertheless, another precondition of their spectral shape is the small diffusion coefficient they adopt, which is an order of magnitude smaller than ours. We have explained in F17 that if we use our diffusion coefficient with their injection spectral parameters, the predicted $e^- + e^+$ flux of Vela X is too large even in sub-TeV, and has a serious contradiction with the AMS-02 data. We should also point out that the total leptonic energy of 6.8×10^{48} erg may be a too large value, since the spin-down luminosity of Vela X given by the ATNF catalog is 6.92×10^{36} erg, corresponding to a spin-down energy of merely 5×10^{48} erg. Besides, the four years of observation of Fermi-LAT and the radio data of Vela X derive a total leptonic energy of 9×10^{47} erg (Grondin et al. 2013). This may be regarded as the upper limit of the leptonic injection energy.

Here we present two scenarios based on different treatments to Vela X: the one is the model given by Hinton et al. (2011) with an injection age of 3 kyr; in the other one, we adopt the diffusion coefficient of our own. For the later, a small leptonic injection energy is indispensable to avoid the conflict with the present $e^- + e^+$ measurements. We set an injection energy of 10^{47} erg and a smaller injection age of 1 kyr for the second model. The predicted $e^- + e^+$ spectra and anisotropies are shown in Fig. 5. For the first model, Vela X

produces a prominent enough feature in the $e^- + e^+$ spectrum, and the predicted anisotropy is not constrained by the upper limits of Fermi-LAT. The steep spectrum of Vela X should be ascribed to the much smaller diffusion coefficient. Alternatively, a very hard injection spectral index can also lead to a steep spectral feature. The second model in Fig. 5 is similar with the previous model of Vela YZ because of the similarity of their parameters.

3.2.3 Cygnus Loop

Another famous nearby SNR—Cygnus Loop—does not appear in the preceding part of the text due to its very low cut-off energy (72 GeV) given by the multi-band fitting in F17. However, there is no available X-ray spectrum of the global region of Cygnus Loop, so the fitted cut-off energy may not be so compelling. If we calculate the cut-off energy of Cygnus Loop with evolution model of SNR (Yamazaki et al. 2006), it should be in the TeV region. Then Cygnus Loop may become a prominent TeV electron contributor. In this model, we keep the parameters of Cygnus Loop fitted in F17, except for the cut-off energy. The size of Cygnus Loop is approximately 200 arcmin, then a distance of 540 pc corresponds to a radius of 15 pc. The velocity of shock wave can be estimated by $0.4\,R/t$ (Sushch et al. 2011), where R is the radius of the shell and t is the age the SNR. We derive a shock velocity of 6×10^7 cm s^{-1}, and the magnetic field given by the multi-band fitting is 9.7 μG, so the cut-off energy is estimated to be approximately 8 TeV. We set a release time of 7 kyr, corresponding to an injection age of 3 kyr. The $e^- + e^+$ spectrum and corresponding anisotropy are presented in Fig. 6. The spectral feature generated by Cygnus Loop is prominent, since the distance of Cygnus Loop is larger compared with Vela and so its spectrum can stand out from the background. We also find the anisotropy of this model only conflicts slightly with the upper limits of Fermi-LAT, compared with the model of Vela YZ and the second scenario of Vela X.

From all the models above, we obtain the constraint on possible TeV spectral features with the restriction of Fermi-LAT: the potential feature should be steep like the first case of Vela X, or it should appear in high energy region of $E > 5$ TeV. The corresponding physical conditions are: a very small diffusion coefficient, or a very hard injection spectral index, or a relatively far distance of the source. Another obvious result is that the anisotropies of all these TeV models can be detected by HERD. If the anisotropy is detected along with a spectral feature in the future, we may even give constraints on the astrophysical models. For example, assuming a prominent feature is detected in the TeV region, and the $\boldsymbol{n}_{\rm max}$ of the intensity distribution points at the location of Cygnus Loop in the corresponding energies. This would indicates that Cygnus Loop should be the source accounting for this spectral feature. Then as we described above, the electron release time of Cygnus Loop can be derived from the spectral shape, which is a parameter that can hardly be determined by electromagnetic observations.

4 DISCUSSION

4.1 Multi-PWN Model

Although the *Monogem Ring* model and the *Loop I (NPS)* model can explain the AMS-02 data and their anisotropies are entirely under the upper limits of Fermi-LAT, they predict a too steep spectral cut at 1 TeV compared with all those TeV measurements. The reason is that all the local sources in sub-TeV—MR, Loop I, and Geminga—begin to descend just below 1 TeV in the spectrum. Geminga has the sharpest decline due to its relatively old age. Here we test a model that consists of a group of PWNe, instead of the case of a single PWN applied above. Young member(s) of the PWN group may help to contribute to the flux around 1 TeV.

We divide the energy range from 10 GeV to 1 TeV into four bins with equal length in logarithmic scale. For each bin, we calculate the integrated positron flux for all the PWNe in our sample, with a uniform spectral index of 1.8. Then all the PWNe are ranked by their integrated flux in each bin. We sum their rank of the four bins for each PWN individually, and the ten with the smallest summed rank are selected as our candidates. They are: J0940-5428, B1055-52, J0633+1746 (Geminga), B0355+54, B1001-47, B0656+14 (Monogem), J0538+2817, J1732-3131, J2043+2740, B1742-30.

We replace Geminga with the ten PWNe in the *Loop I (NPS)* model, to fit the AMS-02 data. The spectral index and conversion efficiency of each PWNe are set to be free, and the cut-off energy is fixed at 2 TeV for all the PWN members. Other parameters in the model remain unchanged as given in Table 3. In the new fitting procedure, the $\eta_{\rm pwn}$ of six PWNe converge to zero, which indicates the other four sources are enough to explain the AMS-02 data. We present the fitting result along with the information of these four PWNe in Table 4. The leptonic spectra of the multi-PWN model and the anisotropy of $e^- + e^+$ are shown in Figure 7. We find that the spectral break in 1 TeV is milder compared with the original *Loop I (NPS)* model, and is in a better consistency with current measurements. Besides, the $e^- + e^+$ anisotropy of this multi-PWN model is also under all the upper limits of Fermi-LAT.

The flux increase in $\sim$ 1 TeV owes much to the source J0940-5428 which has a significant contribution up to several TeV. J0940-5428 is a Vela-like pulsar due to its fast spinning, relatively young age, and large spin-down luminosity (Crawford & Tiffany 2007). The ATNF catalog now provides a much closer distance of 0.38 kpc for J0940-5428, compared with the old estimation of $\sim$ 4 kpc. This is crucial to update the status of J0940-5428 in the $e^{\pm}$ spectrum. However, we still have much less knowledge of J0940-5428 at present than well-studied sources like Geminga. Researches have shown that J0940-5428 may not be surrounded by an observable synchrotron nebula as the case of Vela X or Geminga (Wang et al. 2014).

4.2 The Case of Featureless TeV Spectrum

Since the contributors of TeV $e^{\pm}$ are few, remarkable spectral structures are often expected. However, the latest preliminary $e^- + e^+$ spectrum of H.E.S.S indicates no prominent feature up to $\sim$ 20 TeV (Kerszberg et al. 2017). If the

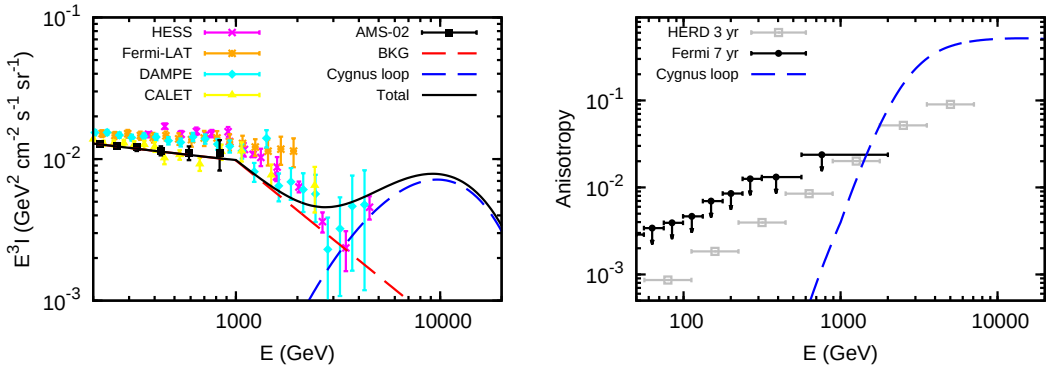

Figure 6. Cygnus Loop overlays on *Loop I (NPS)* model. The cut-off energy of Cygnus Loop is 8 TeV, other injection parameters are kept as the fitted value in F17: $\gamma = 1.99$, $Q_0 = 10^{50}$ GeV^{-1}. Left: the $e^- + e^+$ spectrum compared with experimental data; right: the corresponding anisotropy, upper limits of Fermi-LAT, and expected detection ability of HERD.

Name	$l(^\circ)$	$b(^\circ)$	r(kpc)	t(kyr)	W_p (10^{49} erg)	γ_pwn	η_pwn
J0940-5428	277.5	−1.3	0.38	42	1.34	1.5	0.036
Geminga	195.1	+4.3	0.25	342	1.23	2.0	0.88
B1001-47	276.0	+6.1	0.37	220	0.480	2.0	0.78
J2043+2740	70.6	−9.2	1.48	1200	25.8	2.0	0.38

Table 4. Members of the Multi-PWN model in Section 4.1. Their position, distance, and age are referred to the ATNF catalog. The last two columns are given by the fitting described in Section 4.1 (the upper and lower bounds of γ_PWN are set to be 2.0 and 1.5 in the fitting process).

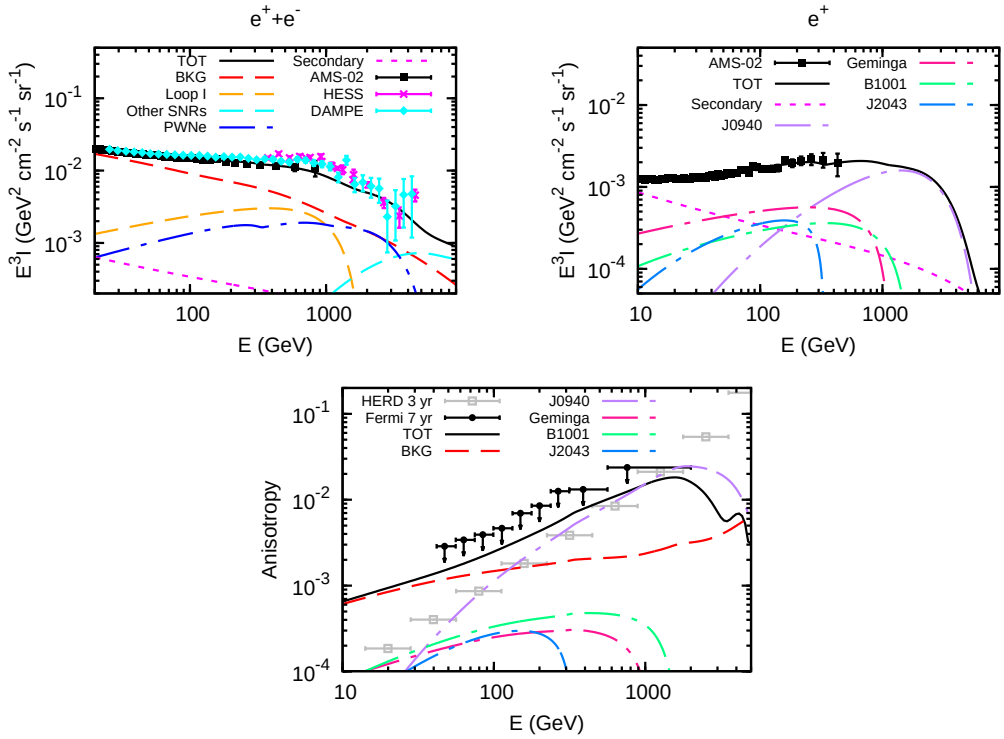

Figure 7. Same as the *Loop (NPS)* model in Section 3.1, but replace the single PWN with a group of PWNe. The positron spectrum of each PWN is shown in the top right.

TeV $e^- + e^+$ spectrum is indeed proved to be featureless in the future, we can hardly discriminate local sources by the $e^- + e^+$ spectrum. In this case, the measurement of anisotropy should be the most important tool of investigating the origin of TeV $e^{\pm}$. Here we discuss the possibility of detecting the anisotropy for a $e^- + e^+$ spectrum with no prominent feature.

As an example, we add Cygnus Loop on a break power-law background to accommodate the preliminary spectrum of H.E.S.S. The spectral index of the background is set to be -3.17 and -3.8 in the region below and above 1 TeV, respectively. The normalization of Cygnus Loop is assumed to be 15% of the case in Section 3.2, to ensure no prominent feature in the total spectrum. The anisotropy is still assumed to be dominated by Cygnus Loop. The spectrum and anisotropy of this case are shown in Fig. 8. As can be seen, the slight spectral bump produced by Cygnus Loop is within the error band of H.E.S.S. At the same time, the anisotropy is hopeful to be detected by HERD above ~ 5 TeV.

5 CONCLUSION

In this paper, we first use the latest anisotropy result of Fermi-LAT to test local source models aimed to explain the leptonic data of AMS-02. Our results show that the anisotropy spectrum of the *Vela YZ* model reaches the exclusion limit at 95% C.L. given by Fermi-LAT, which means the result of Fermi-LAT disfavors Vela YZ as the dominant local SNR in the sub-TeV region. The other two models, where Monogem Ring or Loop I (NPS) plays the role of the dominant local SNR, remain safe under the restriction of the Fermi-LAT result. This implies the extra electron excess in sub-TeV should be explained by a relatively old source. The next generation instrument HERD is expected to have a better sensitivity than Fermi-LAT. We then estimate the capability of anisotropy detection of HERD, and find HERD is sensitive enough to discriminate between the *Monogem Ring* model and the *Loop I (NPS)* model, as the predicted angular intensity maps of these two scenarios are remarkably different. We also point out that the SNR background has a considerable contribution to the anisotropy which is even larger than that of some discrete local sources like Geminga, so this component should not be neglected in the calculation, especially in sub-TeV.

Since fewer local sources can contribute significantly to the TeV $e^- + e^+$ spectrum, spectral features are expected in the TeV region. We discuss several cases of remarkable features in TeV by adding dominant local sources on a break power-law background. The predicted anisotropies of some cases conflict with the upper limits of Fermi-LAT, and we find the conditions for a remarkable TeV feature which satisfies the anisotropy constraint by Fermi-LAT: if Vela YZ or Vela X is the dominant TeV source, a considerable electron injection delay (10 kyr) is necessary, and a much smaller diffusion coefficient than usual or a very hard injection spectrum is needed to avoid the anisotropy constraint; a dominant source with relatively farther distance is also a solution, like Cygnus Loop, which can produce a spectral feature in higher energies (> 5 TeV) considering an injection delay. Moreover, the predicted anisotropies of all those TeV models can be detected by HERD. So if we could detect remarkable spectral features along with the anisotropy in the future, we may even give constraints on some physical parameters, such as the injection delay of the source, or the diffusion coefficient of high energy $e^{\pm}$.

Besides, the latest preliminary $e^- + e^+$ spectrum of H.E.S.S indicates no prominent feature in the TeV region. We discuss a case with no significant structure in the $e^- + e^+$ spectrum, and find that HERD will likely detect the anisotropy of a local source in this case. Thus, the possibility of ascertaining the local source is still retained even in the case of a featureless $e^- + e^+$ spectrum, and HERD may play an important role in the study of the origin of high energy CR $e^{\pm}$.

ACKNOWLEDGEMENT

We thank Ming Xu for providing the simulated performance of HERD. This work is supported by the National Key Program for Research and Development (No. 2016YFA0400200) and by the National Natural Science Foundation of China under Grants No. U1738209, 11475189, 11475191, and is supported in part by the CAS Center for Excellence in Particle Physics (CCEPP).

REFERENCES

Abdollahi, S., Ackermann, M., Ajello, M., et al. 2017, Physical Review Letters, 118, 091103
Adriani, O., Barbarino, G. C., Bazilevskaya, G. A., et al. 2009, Nature , 458, 607
Aguilar, M., Aisa, D., Alvino, A., et al. 2014, Physical Review Letters, 113, 121102
Aguilar, M., Aisa, D., Alpat, B., et al. 2015, Physical Review Letters, 114, 171103
Aharonian, F., et al. 2008, Physical Review Letters, 101, 261104
Alvarez, H., Aparici, J., May, J., & Reich, P. 2001, Astron. Astrophys. , 372, 636
Atoyan, A. M., Aharonian, F. A., & Völk, H. J. 1995, Phys. Rev. D , 52, 3265
Borken, R. J., & Iwan, D.-A. C. 1977, Astrophys. J. , 218, 511
Casandjian, J.-M., Grenier, I., & for the Fermi Large Area Telescope Collaboration. 2009, ArXiv e-prints, arXiv:0912.3478
Chang, J., Adams, J. H., Ahn, H. S., et al. 2008, Nature , 456, 362
Crawford, F., & Tiffany, C. L. 2007, Astron. J. , 134, 1231
DAMPE Collaboration. 2017, Nature , 552, 63
de Jager, O. C., Slane, P. O., & LaMassa, S. 2008, Astrophys. J. Lett. , 689, L125
Delahaye, T., Lavalle, J., Lineros, R., Donato, F., & Fornengo, N. 2010, Astron. Astrophys. , 524, A51
Di Mauro, M., Donato, F., Fornengo, N., Lineros, R., & Vittino, A. 2014, J. Cosmol. Astropart. Phys. , 4, 006
Dong, Y.-W., Xu, M., Wang, Z.-G., et al. 2017, 35th International Cosmic Ray Conference, Bexco, Busan, Korea, 301
Dorfi, E. A. 2000, Astrophys. Space Sci. , 272, 227
Egger, R. J., & Aschenbach, B. 1995, Astron. Astrophys. , 294, L25
Fang, K., Wang, B.-B., Bi, X.-J., Lin, S.-J., & Yin, P.-F. 2017, Astrophys. J. , 836, 172
Feng, L., Yang, R.-Z., He, H.-N., et al. 2014, Physics Letters B, 728, 250
Ginzburg, V. L., & Syrovatskii, S. I. 1964, The Origin of Cosmic Rays

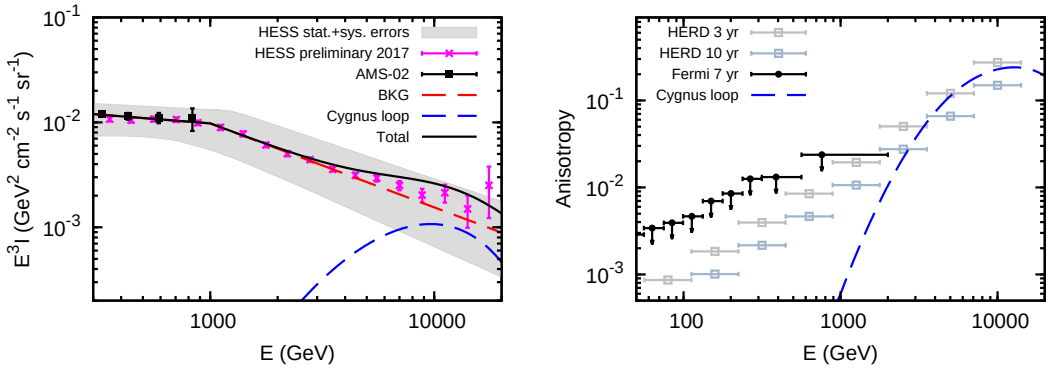

Figure 8. An example with no remarkable feature in the TeV $e^- + e^+$ spectrum. The background of this model is a break power-law spectrum with a spectral softening from -3.17 to -3.8 at 1 TeV.

Grondin, M.-H., Romani, R. W., Lemoine-Goumard, M., et al. 2013, Astrophys. J. , 774, 110

Han, J. L., & Qiao, G. J. 1994, Astron. Astrophys. , 288, 759

Hinton, J. A., Funk, S., Parsons, R. D., & Ohm, S. 2011, Astrophys. J. Lett. , 743, L7

Kerszberg, D., Kraus, M., Kolitzus, D., et al. 2017, 35th International Cosmic Ray Conference, Bexco, Busan, Korea

Kobayashi, T., Komori, Y., Yoshida, K., & Nishimura, J. 2004, Astrophys. J. , 601, 340

Li, X., Shen, Z.-Q., Lu, B.-Q., et al. 2015, Physics Letters B, 749, 267

Lin, S.-J., Yuan, Q., & Bi, X.-J. 2015, Phys. Rev. D , 91, 063508

Linden, T., & Profumo, S. 2013, Astrophys. J. , 772, 18

Lorimer, D. R. 2004, in IAU Symposium, Vol. 218, Young Neutron Stars and Their Environments, ed. F. Camilo & B. M. Gaensler, 105

Manchester, R. N., Hobbs, G. B., Teoh, A., & Hobbs, M. 2005, Astron. J. , 129, 1993

Manconi, S., Di Mauro, M., & Donato, F. 2017, J. Cosmol. Astropart. Phys. , 1, 006

Pato, M., Lattanzi, M., & Bertone, G. 2010, J. Cosmol. Astropart. Phys. , 12, 020

Plucinsky, P. P. 2009, in American Institute of Physics Conference Series, ed. R. K. Smith, S. L. Snowden, & K. D. Kuntz, Vol. 1156, 231–235

Plucinsky, P. P., Snowden, S. L., Aschenbach, B., et al. 1996, Astrophys. J. , 463, 224

Rishbeth, H. 1958, Australian Journal of Physics, 11, 550

Schlickeiser, R., & Ruppel, J. 2010, New Journal of Physics, 12, 033044

Shen, C. S. 1970, Astrophys. J. Lett. , 162, L181

Sofue, Y., Hamajima, K., & Fujimoto, M. 1974, Publications of the Astronomical Society of Japan, 26, 399

Sushch, I., & Hnatyk, B. 2014, Astron. Astrophys. , 561, A139

Sushch, I., et al. 2011, Astron. Astrophys. , 525, A154

Wang, Z., Ng, C.-Y., Wang, X., Li, A., & Kaplan, D. L. 2014, Astrophys. J. , 793, 89

Weiler, K. W., & Panagia, N. 1980, Astron. Astrophys. , 90, 269

Yamazaki, R., Kohri, K., Bamba, A., et al. 2006, Mon. Not. Roy. Astron. Soc. , 371, 1975

Yuan, Q., Lin, S.-J., Fang, K., & Bi, X.-J. 2017, Phys. Rev. D , 95, 083007

Zhang, S. N., Adriani, O., Albergo, S., et al. 2014, in Proc. SPIE, Vol. 9144, Space Telescopes and Instrumentation 2014: Ultraviolet to Gamma Ray, 91440X

Zhang, S.-N., et al. 2017, 35th International Cosmic Ray Conference, Bexco, Busan, Korea, 301